

Kinematic rupture model of the February 6th 2023 Mw7.8 Turkey earthquake from a large set of near-source strong motion records combined by GNSS offsets reveals intermittent supershear rupture

Bertrand Delouis¹, Martijn van den Ende¹, and Jean-Paul Ampuero¹

¹Université Côte d'Azur, CNRS, IRD, Observatoire de la Côte d'Azur, Géoazur

April 30, 2023

1 **Title:**

2 **Kinematic rupture model of the February 6th 2023 Mw7.8 Turkey earthquake from a large set**
3 **of near-source strong motion records combined with GNSS offsets reveals intermittent**
4 **supershear rupture**

5

6 **Authors:**

7

8 Bertrand DELOUIS (corresponding author)

9 Université Côte d'Azur, CNRS, IRD, Observatoire de la Côte d'Azur, Géoazur, 250 rue Albert

10 Einstein, 06560 Valbonne, France

11

12 Martijn VAN DEN ENDE

13 Université Côte d'Azur, CNRS, IRD, Observatoire de la Côte d'Azur, Géoazur

14

15 Jean-Paul AMPUERO

16 Université Côte d'Azur, IRD, CNRS, Observatoire de la Côte d'Azur, Géoazur

17

18 The authors acknowledge there are no conflicts of interest recorded

19 **Key points**

20 **1. We infer the kinematic slip history of the 2023 M7.8 Turkey earthquake from**
21 **unprecedentedly-dense near-fault strong motion data**

22

23 **2. We identify several portions of the East Anatolian Fault where the rupture is**
24 **transiently supershear**

25

26 **3. We associate transitions to supershear speed with regions of reduced fault slip, which**
27 **could relate to failure of local rupture barriers**

28

29 **Abstract**

30 The 2023 M7.8 SE Turkey earthquake was recorded by an unprecedentedly large set of strong
31 motion stations very close to its rupture, opening the opportunity to observe the rupture process
32 of a large earthquake with fine resolution. Here, the kinematics of the earthquake source is
33 inferred by finite source inversion based on strong motion records and coseismic offsets from
34 permanent GNSS stations. The strong motion records at stations NAR and 4615, which are closest
35 to the splay fault where the rupture initiated and which were previously interpreted as containing
36 the signature of supershear rupture speeds, are successfully modeled here by a sub-shear rupture
37 propagating unilaterally to the NE. Once the rupture on the splay fault reaches the East Anatolian
38 Fault (EAF), it propagates on the EAF bilaterally, extending about 120 km NE and 180 km SW. To

39 the South, the depth extent of the rupture decreases as it passes a bend of the EAF. While the
40 rupture velocity remains globally sub-shear along the EAF, we identify several portions of the fault
41 where the rupture is transiently supershear. The transitions to supershear speed coincide with
42 regions of reduced fault slip, which suggests supershear bursts generated by failure of local
43 rupture barriers. Towards the SW termination, the rupture encircles an asperity before its failure,
44 which is a feature that has been observed only on rare occasions. This unprecedented detail of
45 the inversion was facilitated by the proximity to the fault and the exceptional density of the
46 accelerometric network in the area.

47 **Introduction**

48 The February 6, 2023 (01H17 UTC) earthquake of moment magnitude (M_w) 7.8 in SE Turkey
49 (Pazarcık, Kahramanmaraş, Türkiye) involved three major fault segments well differentiated by
50 location and orientation (e.g. Melgar et al., 2023). The rupture started on a fault branch that
51 splays off from the East Anatolian Fault (EAF) and runs adjacent to the city of Narli where strong
52 motion stations 4615 and NAR are located (**Figure 1**). This splay fault is sometimes referred to as
53 the Narli Fault, however Melgar et al. (2023) referred to it as the Nurdağı-Pazarcık Fault; it will be
54 called hereafter the splay fault (SPF). The rupture later propagated on two segments of the EAF.

55 In principle the time-dependent earthquake rupture process can be constrained by seismological
56 data, but in practice such efforts are often limited by the scarcity of near-source recordings. Our
57 objective here is to take advantage of the existence of numerous strong motion stations in the
58 immediate vicinity of the ruptured fault segments to determine with fine resolution the
59 characteristics of the rupture in space and time. GNSS static coseismic offsets are also used to

60 further constrain the spatial distribution of slip. Previous studies (USGS 2023; Melgar et al. 2023)
61 have highlighted the general characteristics of the earthquake by combining different types of
62 data, but using only a limited number of strong motion stations (< 15). So far, the potential for
63 source inversion enabled by the dense strong motion network installed in the area by the Turkish
64 Disaster and Emergency Management Authority (AFAD) has only been partially exploited. In
65 particular, the signals from two stations very close to the splay fault (NAR and 4615) were
66 proposed to contain evidence for supershear rupture on this branch of the rupture (Rosakis et al.,
67 2023), but these signals have not yet been modeled by source inversion studies. Moreover, earlier
68 studies of this earthquake reported sub-shear speeds on the EAF. Here, exploiting the complete
69 dataset we gain further insights into the evolution of rupture speed during this earthquake.

70 In this study we model a large set of 31 strong motion stations, including the closest ones to the
71 rupture segments, plus the available horizontal coseismic offsets from 20 GNSS stations. These
72 data are inverted jointly to constrain the parameters of a kinematic source model of the Mw 7.8
73 earthquake. Our inversion results provide a view of the rupture process, including the spatial
74 variability of rupture speed, with an unprecedented level of resolution.

75

76 **Strong motion data**

77 A very dense set of near-field strong motion records (3 components: NS, EW and vertical) from
78 the Turkish National Strong Motion Network have been made publicly available by the Disaster
79 and Emergency Management Authority (AFAD) through the Turkish Accelerometric Database and
80 Analysis System (TADAS). We selected 31 stations covering the entire rupture zone, including

81 stations located very close to the ruptured segments (**Figure 1**). Signal processing includes
82 removal of the pre-event mean amplitude, double integration to displacement, and bandpass
83 filtering. The low frequency cutoff varies between 0.005 and 0.06 Hz, depending on the amount
84 of long-period noise observed after the double integration. The high-frequency cutoff is set to 0.3
85 Hz, corresponding to the highest frequency at which we judge waveforms can be modeled
86 adequately using a simple velocity model for wave propagation. Synthetic seismograms are
87 computed by the wavenumber integration method of Bouchon (1981) adopting a 1D velocity
88 model (**Table S1** in the electronic supplement to this article) derived from the regional velocity
89 model determined by Güvercin et al. (2022). On the fault segment located in the immediate
90 vicinity of the NAR and 4615 stations (segment 1bis, see model description in Section “Kinematic
91 model, inversion method, and constraints on rupture parameters”), we computed synthetic
92 waveforms using exact expressions for the displacement field at the surface of a uniform elastic
93 half-space (Johnson, 1974), including near-field waves, as implemented in Legrand (1995).

94 **GNSS data**

95 Coseismic static offsets obtained from GNSS time series were made available by the Nevada
96 Geodetic Laboratory for stations from the CORS (Continuous Operating Reference Stations)
97 network, calculated with final orbits from the NASA Jet Propulsion Laboratory (JPL) on 26
98 February 2023. We selected the horizontal offsets at 20 stations closest to the rupture zone
99 (**Figure 1**). We calculated synthetic static displacements using the formulation of Savage (1981)
100 for dislocations in an elastic half-space

101

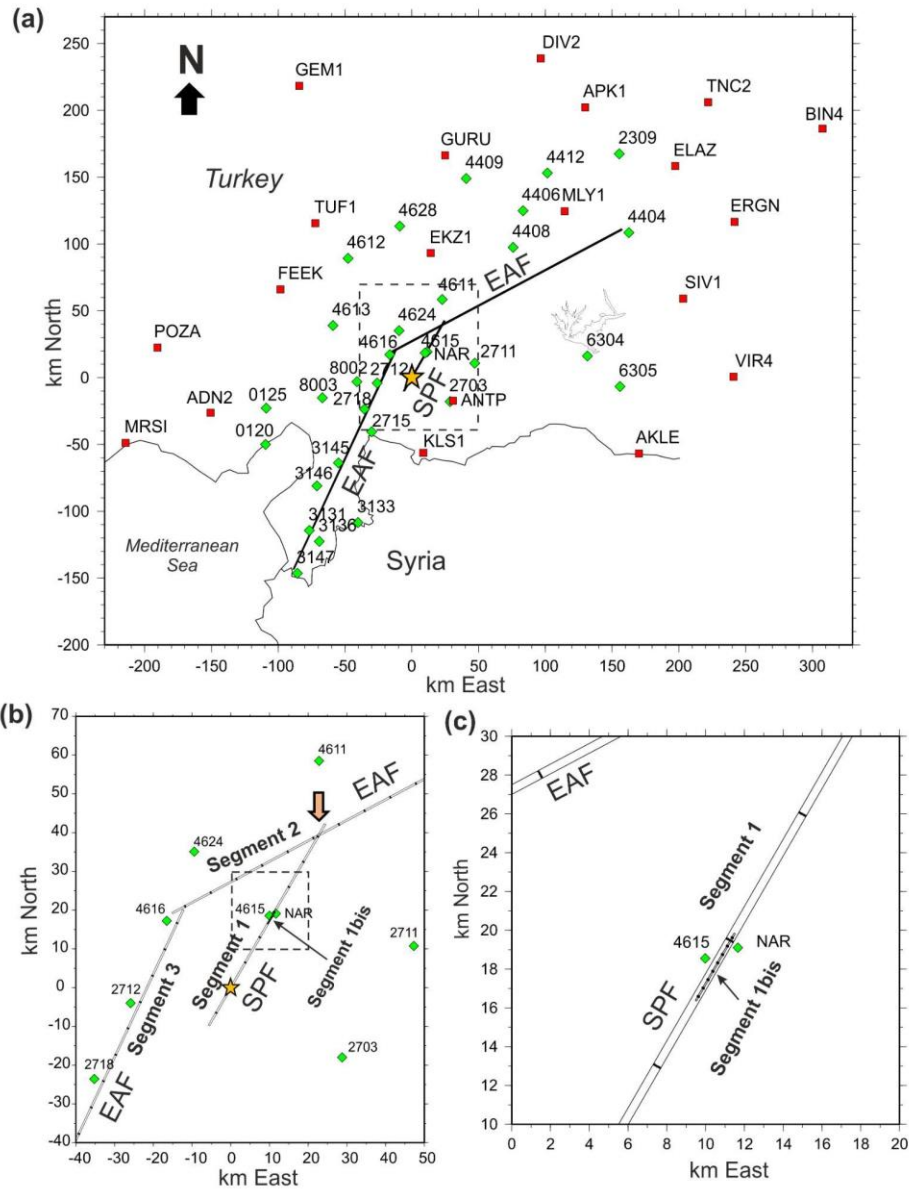
102 **Kinematic model, inversion method, and constraints on rupture parameters**

103 We define the kinematic model and conduct the finite source inversion following a similar
104 approach to that used by Delouis et al. (2002) to model the 1999 Izmit (Mw 7.6) earthquake. The
105 rupture is represented by rectangular fault segments, subdivided into small dislocation surfaces
106 (subfaults) to model static surface displacements, and represented by a point source at their
107 center to model seismic waveforms. The model and subfault dimensions are provided in **Table 1**
108 and their surface projection is shown in **Figure 1**.

109 The local source time function associated with each point source is represented as the sum of
110 three isosceles triangular moment rate functions, mutually overlapping, each with a total
111 duration of 4 s. Two bounding rupture velocities, called V_{rmin} and V_{rmax} , limit the rupture onset
112 times along the fault by enforcing the constraint $V_{rmin} \leq \text{dist_subfault} / \text{onset_time} \leq V_{rmax}$.
113 Here we define dist_subfault as the distance along the fault segments between the subfault
114 center and the rupture initiation point. The latter is set as the hypocenter for segments 1 and
115 1bis, and as the junction between SPF and EAF for segments 2 and 3 (**Figure 1**). This constraint
116 has the following physical meaning: at any given location along the faults, the average rupture
117 slowness (defined as the rupture slowness spatially averaged over horizontal along-fault distance
118 between the rupture initiation point and the given location) is constrained to lie between
119 $1/V_{rmax}$ and $1/V_{rmin}$. Within the constrained range, the rupture onset times are allowed to vary
120 freely, thus the rupture speeds at any point of the fault (called hereafter the local rupture speed)
121 can lie beyond the $V_{rmin} - V_{rmax}$ range (see **Figure S1** for an illustration, in the electronic
122 supplement to this article).

123 The inverted parameters are, for each subfault, the rupture onset time, the amplitudes of the
124 triangular functions, and the rake angle. The inversion itself is carried out with a simulated
125 annealing algorithm. The cost function to be minimized is a weighted sum of the normalized RMS
126 (root mean square) misfit functions for each dataset, plus a seismic moment minimization
127 function and a smoothing function.

128 The strong motion stations are located much closer to the rupture than the GNSS stations (**Figure**
129 **1a**), thus they are more sensitive to fine details of the rupture and more difficult to model.
130 Consequently, a lower weight ($w=0.4$) is assigned to the GNSS data than to the strong motion data
131 ($w=1.0$). The weights assigned to the seismic moment minimization and smoothing functions are
132 adjusted so as not to incorporate excess seismic moment for little gain in data fit, and to avoid
133 incorporating a level of detail in the model that is poorly constrained by the data.



134

135

136

137

138

139

140

Figure 1. (a) Overview map showing the strong motion (green diamond) and GNSS (red squares) stations used in this study, with corresponding names. Thick black line: surface trace of the fault model. Orange star: epicenter of the mainshock (37.22°N, 37.025°E, this study) at the origin of the coordinates (0,0). The dashed box indicates the zone (b). **(b)** Close-up of the epicentral area. Thin lines with small dots show the fault model with the center of the point sources,

141 projected on the earth surface. The names of the fault segments are shown. The
142 dashed frame indicates the zone (c). Orange arrow: junction between segment 1-
143 1bis (splay fault) and segment 2 (East Anatolian Fault). **(c)** Close-up of the area
144 where the fault model passes between the strong motion stations 4615 and NAR
145 and where a finely discretized fault segment 1bis is used. SPF: splay fault; EAF:
146 East Anatolian Fault.

147

148 The hypocenter has been located by many agencies, systematically more than 15-20 km south of
149 the EAF (e.g. AFAD, KOERI, USGS). As in Melgar et al. (2023), we consider that the hypocenter
150 occurred on a NNE-SSW fault branch, a splay fault (SPF, **Figure 1**) with respect to the EAF. Using
151 P arrival times and a few S arrival times at the nearby strong motion stations, we located the
152 epicenter of the main shock at 37.22°N and 37.025°E, with an estimated uncertainty of less than
153 5 km, using the GRIDSIMLoc nonlinear approach (Delouis et al., 2022). However, the hypocenter
154 depth, ranging from 3 to 20 km, is not well constrained by the arrival times. We used this
155 epicenter to define the rupture initiation point in our kinematic slip model, and tested different
156 hypocenter depths based on the discretization of our rupture model. Finally, the best results were
157 obtained with a hypocenter depth of 12.5 km, but the inversion results are not very sensitive to
158 variations of this parameter within +/- 5 km.

159 The rupture model includes three fault segments, corresponding to the minimum degree of
160 complexity to represent to first order the rupture geometry constrained by satellite imagery,
161 aftershock distribution and field observations (e.g. map from the USGS Turkey Earthquake

162 Emergency Response (Reitmann et al., 2023), and the compilation of documentation on the
163 Kahramanmaraş Supersite science web page, see Data and resources). Segment 1 corresponds to
164 the NNE-SSW trending splay fault hosting the hypocenter. Segments 2 and 3 correspond to the
165 NE-SW segment (striking N62) and NNE-SSW segment (striking N25) of the EAF, respectively
166 (**Figure 1** and **Table 1**). On all segments, we allow the rake to vary by $\pm 45^\circ$ around the central
167 value of 0 corresponding to a dominant left-lateral strike-slip motion (**Table 1**). In initial
168 inversions, we allowed the dip of fault segments to vary between 80 and 90 degrees, to the NW
169 or SE, but we observed no real impact on the data modeling. Since the data do not appear to be
170 very sensitive to the choice of dip when it is close to vertical, we set it at 89° to the SE for all
171 segments.

172

173 **Preliminary constraints on rupture speeds**

174 Two accelerometer stations were the focus of special attention, as their positioning is of primary
175 importance to constrain the initial phase of the rupture on the SPF. These are stations 4615 and
176 NAR, the closest ones to the epicenter. Between these two stations, separated by only 1.8 km,
177 surface breaks have been identified, with displacements of the order of 2.6 to 2.8 m (**Figure S2** in
178 the electronic supplement to this article). This is strong evidence that these stations are located
179 on opposite sides of the ruptured splay fault.

180 A major pulse, clearly visible on the velocity seismograms and marked by a maximum
181 displacement of 210 cm southward at station 4615 and 90 cm northward at station NAR, starts
182 about 4.8 s after the first arrival of the P-wave at these two stations (**Figure S3** in the electronic

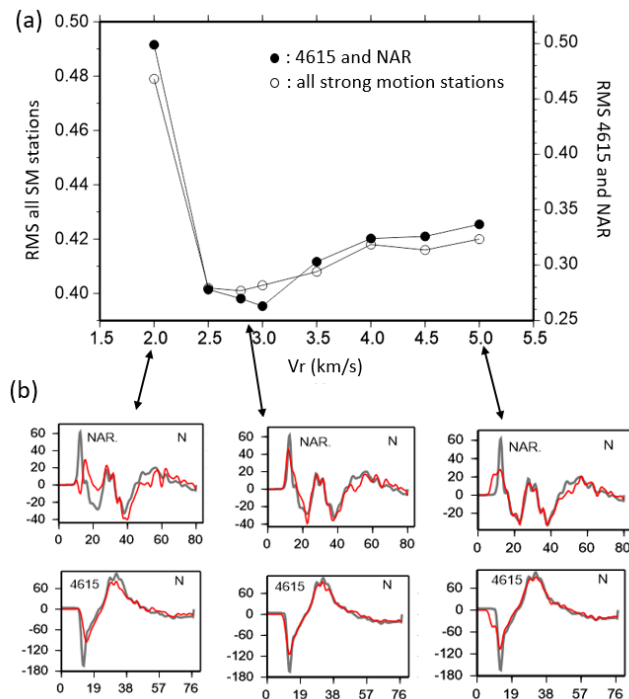
183 supplement to this article). We interpret this part of the signal as being produced by the left-
184 lateral surface faulting between the two stations. The rupture, located less than one kilometer
185 from the stations, moves 4615 southward and NAR northward. The reversal of the direction of
186 displacement and the magnitude of the displacement observed at these two stations so close to
187 each other appears to be the direct signature of a local fault offset of at least 3 m (2.1 + 0.9 m),
188 in agreement with the surface observations (**Figure S2** in the electronic supplement to this
189 article).

190 Modeling the first 15 seconds of the signal following the P-wave onset at stations 4615 and NAR
191 required special effort. We found it necessary to incorporate a finely discretized portion of the
192 fault between the two stations, denoted as segment 1bis (**Table 1** and **Figure 1b-c**). The synthetic
193 seismograms generated by segment 1bis for stations 4615 and NAR were calculated using the
194 exact analytical solution for a homogeneous half-space of Johnson (1974), which is more accurate
195 for very small source-station distances than the numerical approach by wavenumber integration
196 (Bouchon 1981). The homogeneous velocity model assumed has P-wave velocity of 4.90 km/s and
197 S-wave velocity of 2.83 km/s.

198 Rosakis et al. (2023) made observations suggesting that a transition from subshear to supershear
199 rupture velocity (V_r) occurred on SPF between stations 4615 and NAR. To examine the rupture
200 velocity on the splay fault, we performed a series of inversions where V_r on segments 1 and 1bis
201 is fixed to a constant value varying from 2.0 to 5.0 km/s. **Figure 2a** shows the variation of RMS fit
202 of all 31 stations on the one hand, and of the two stations 4615 and NAR on the other hand, as a
203 function of the fixed V_r value. The effect of the choice of V_r on the modeling of the north
204 component of 4615 and NAR is illustrated in **Figure 2b**. Best results are obtained for constant V_r

205 in the range 2.8 to 3.0 km/s, with already good results for $V_r=2.5$ km/s. This indicates that, to
 206 model displacement waveforms in the frequency band used here, it is not necessary for V_r to
 207 transition from sub-shear to supershear. We will come back to this point in the discussion. In our
 208 final inversion, we relax the constraint of a constant V_r on the splay fault by allowing the average
 209 V_r to vary between $V_{rmin} = 2.5$ km/s and $V_{rmax} = 3.3$ km/s.

210



211

212 **Figure 2.** Exploration of the rupture velocity (V_r) on
 213 segments 1 and 1bis. **(a)** RMS waveform misfit value for all
 214 strong motion stations (SM) and for 4615 and NAR only as
 215 a function of fixed constant V_r values. **(b)** North component
 216 waveform fit for NAR and 4615 stations for constant V_r
 217 values of 2.0, 2.8 and 5.0 km/s. Waveforms are in

218 displacement and bandpass filtered between 0.01 and 0.3
219 Hz. Only the north components of NAR and 4615, being the
220 most sensitive to V_r and the most difficult to model, are
221 shown but the inversion is performed with the three
222 components N, E and Z of all strong motion stations.

223 During initial inversions, we observed that slip on segments 1 and 1bis (SPF) could reach 6 m, in
224 disagreement with independent evidence of surface offsets of no more than 3 m along this fault
225 section (**Figure S2** in the electronic supplement to this article). Although it cannot be ruled out
226 that slip at depth may exceed slip at the surface, we noted that the fit of the data was not
227 significantly improved when the maximum slip on these segments increased from 4 to 6 m. In the
228 final inversion the slip on segments 1 and 1bis is limited to 4 m.

229 A delay is imposed to the initiation of the rupture on segment 2 to force the rupture on the EAF
230 to start after the rupture along the SPF has reached the junction with the EAF (**Figure 1b**). We
231 tested delay values (relative to the hypocenter origin time) ranging from 10 to 18 s and retained
232 the value of 14 s which gives the best fit of the data.

233 Regarding the EAF (segments 2 and 3), optimum results are obtained by using $V_{rmin} = 2.0$ km/s
234 and $V_{rmax} = 4.0$ km/s. Expanding the range $V_{rmin} - V_{rmax}$ beyond these limits does not produce
235 a significant improvement in data fit. On segments 2 and 3, the distance considered to constrain
236 V_r is the distance along the fault relative to the SPF-EAF junction (**Figure 1b**), with a time origin
237 corresponding to the start time on segment 2, i.e. 14 s after rupture initiation on segment 1. The
238 maximum allowed slip on the EAF was explored between 5 and 12 m. The improvement in the fit

239 of the data becomes small for a maximum slip greater than 7 to 8 m, and slip was limited to 8 m
 240 in the final inversion. However, the maximum slip on the EAF is not constrained with an
 241 uncertainty better than +/- 1 to 2 m.

242

| Segment | Strike (°) | Dip (°) | Central rake (°) | L (km) | W (km) | Δl (km) | Δw (km) | Vrmin (km/s) | Vrmax (km/s) |
|---------|------------|---------|------------------|--------|--------|-----------------|-----------------|--------------|--------------|
| 1 | 30 | 89 | 0 | 60 | 25 | 7.5 | 5.0 | 2.5 | 3.3 |
| 1bis | 30 | 89 | 0 | 4 | 5 | 0.5 | 1 | 2.5 | 3.3 |
| 2 | 62 | 89 | 0 | 195 | 25 | 7.5 | 5.0 | 2.0 | 4.0 |
| 3 | 25 | 89 | 0 | 180 | 25 | 7.5 | 5.0 | 2.0 | 4.0 |

243

244 **Table1.** Fixed parameters for the fault segments of the kinematic rupture model. L:
 245 length; W: width; Δl and Δw subfault length and width. Vrmin and Vrmax: bounding
 246 rupture velocities. The top of all segments is located at the free surface.

247

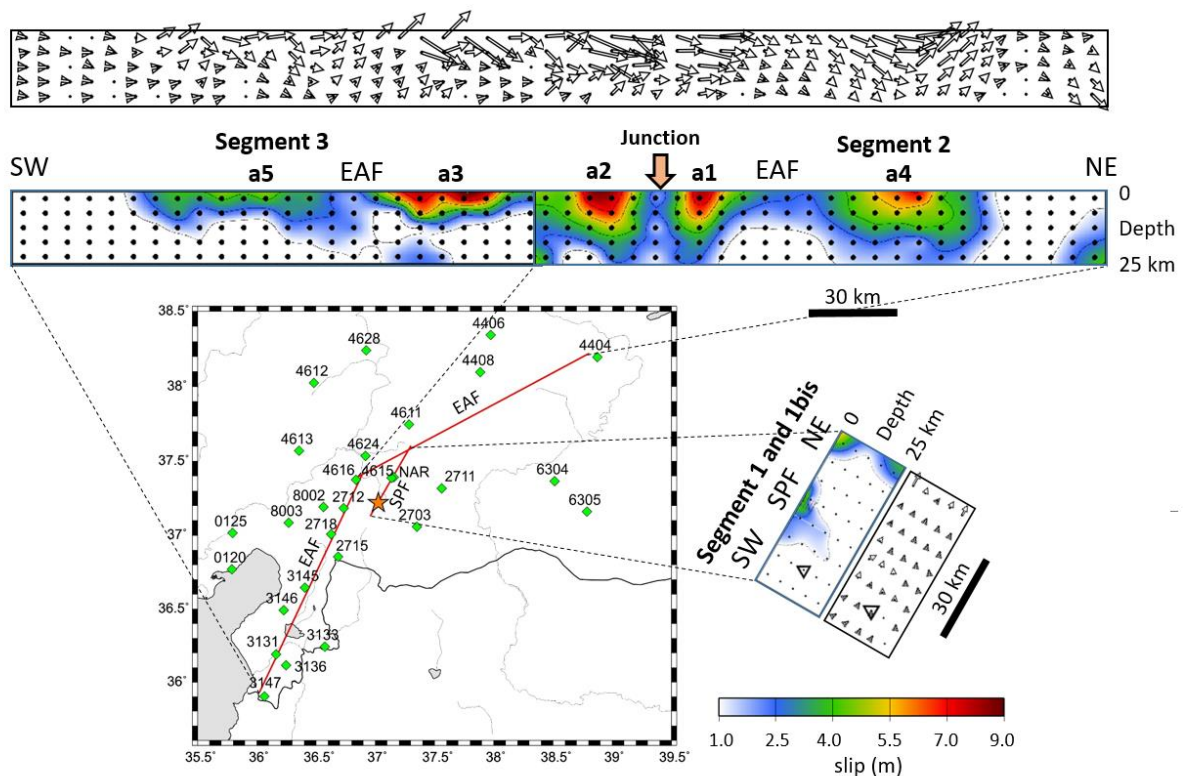
248 **Final slip model and rupture timing**

249 We present here the final slip model resulting from the joint inversion of the strong motion and
 250 GNSS static data. The spatial distribution of slip is shown in **Figure 3**. The spatial and temporal
 251 distribution of the slip is presented on **Figures 4, 5, 6, and 7** separately for the SPF (segments 1
 252 and 1bis) and for the EAF (segments 2 and 3).

253 On the SPF, the rupture is unilateral to the NNE. The total slip is limited at the hypocenter and
 254 south of it. Beyond about 15-20 km NE from the epicenter, slip is mainly localized near the surface,
 255 between stations 4615 and NAR, and at the end of the SPF at its junction with the EAF. From the
 256 junction on, the rupture propagates bilaterally on the EAF, for about 120 km to the NE and 180
 257 km to the SW. On segment 2 slip reaches 20-25 km depth, whereas on segment 3 it is shallower,

258 localized above 10 km depth. Along the whole rupture, the maximum slip is found close to the
 259 surface. It reaches our maximum allowed value of 8 m on both segments of the EAF.

260 On the EAF, slip at the junction with the splay fault is small, but it may be partially compensated
 261 by slip at the NNE termination of the splay fault. The slip observed at the NE end of segment 2 is
 262 likely an artifact, possibly related to a geometric complexity of the rupture not taken into account
 263 in the model.



264

265 **Figure 3.** Slip distribution from the joint inversion of strong motion and
 266 GNSS data on the three segments of the kinematic model, and relation with
 267 the map view. SPF: splay fault; EAF East Anatolian Fault. On the map, the
 268 epicenter, the surface trace of the rupture model, and the strong motion
 269 stations are represented by the orange star, the red lines and the green

270 diamonds respectively. The hypocenter on segment 1-1bis (SPF) is marked
271 by the open triangle. The junction between the splay fault (SPF, segment 1)
272 and Segment 2 of the EAF is marked by the orange arrow. a1 to a5: labels
273 for the main slip areas along the EAF. The slip direction is indicated by the
274 open arrows scaled with slip amplitude.

275
276 On the SPF, the rupture propagates horizontally at a near constant rupture velocity of 2.5 to 2.6
277 km/s (**Figure 4a**). In the time interval between 12 and 20 s, the rupture front is faint and difficult
278 to follow on the slip velocity snapshots (**Figure 6a**) and little slip is accumulated (**Figure 6b**). After
279 20 s, larger slip emerges near the junction with the EAF.

280 Along the EAF, the average rupture velocity calculated from the junction with the splay fault
281 remains below 3 km/s along segment 2 and close to 3 km/s over most of segment 3. (**Figure 4b**).
282 However, we identify notable local deviations from this average trend.

283 To analyze the inversion results, we estimate the local rupture speed and acceleration (horizontal
284 apparent values) by tracking the onset of slip on the sub-faults (**Figure 5**). We determine the
285 apparent rupture acceleration, as a function of along-strike distance, that minimizes the
286 difference between the observed position of the rupture front and the double integral of the
287 rupture acceleration, with a mild smoothness constraint on the acceleration. The resulting
288 acceleration is integrated once to obtain the rupture speed along the fault.

289

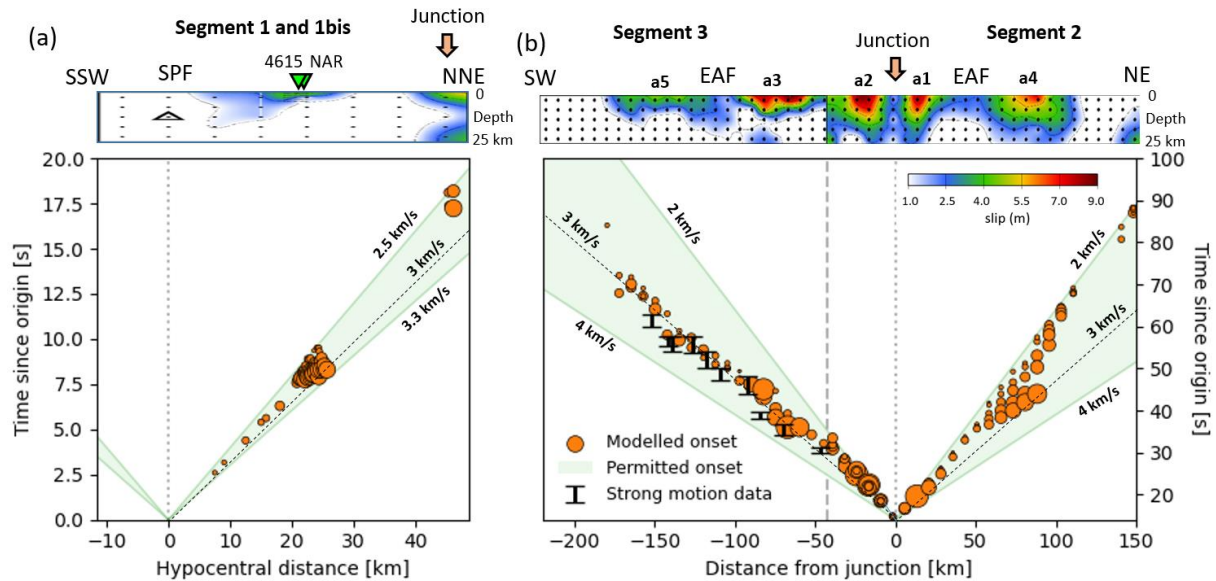
290 Initially and up to a distance of about 30 km from the junction, rupture propagates both to the
291 NE and to the SW at a relatively low speed, between 2 and 2.5 km/s, generating two main slip
292 areas we denote as a1 and a2 (**Figures 4b, 5, and 7**). Then, we observe a pattern common to both
293 rupture directions: after running through a low slip section (gray areas on **Figure 5**), rupture speed
294 increases when entering into the next high slip area (a3, a4, a5), reaching locally a value of 4 km/s
295 or more, maintained over a distance of 20 to 30 km (red F markers on **Figure 5c**, and on **Figure**
296 **7a**). This pattern involves multiple transitions from sub-shear to supershear rupture speed along
297 the EAF at the scale of a few tens of kilometers.

298 As an independent verification of the rupture trajectory along Segment 3, we inspected the strong
299 motion waveforms of selected receivers closest to the fault (**Figure S4 in the electronic**
300 **supplement to this article**). The three-component waveforms were bandpass filtered from 1 to 5
301 Hz, after which we computed the amplitude of motion as $A=\sqrt{N^2+E^2+Z^2}$ for components N, E, and
302 Z. The passage of the rupture was clearly visible as a strong pulse in the amplitude time series,
303 the timing of which was manually picked. To acknowledge uncertainty in the onset time due to
304 the emergent onset, an onset time range was selected; this time range is indicated in **Figure 4b**,
305 and verifies the rupture trajectory inferred by source inversion. Notably, the manual picks confirm
306 the existence of brief supershear phases along Segment 3.

307 The lateral progression of the rupture generally takes place first at or near the surface (**Figures 6**
308 **and 7**). There is one notable exception: around the main slip area a5 on segment 3, the snapshots
309 at 56 s of slip velocity and cumulative slip (**Figure 7a and b**, green U mark) show that rupture
310 propagates first at 10-12 km depth, leaving unbroken the shallowest portion of the fault. This
311 shallow part slips a few seconds later (see the next snapshot at 59 s). Such a delayed rupture of

312 an asperity after it has been surrounded by slip has been described by Zhang et al. (2012) for the
 313 2008 Mw 7.9 Wenchuan earthquake in China, and by Meng et al (2018) for the 2015 Mw 8.3
 314 Illapel earthquake in Chile, though here it is observed at a smaller scale.

315

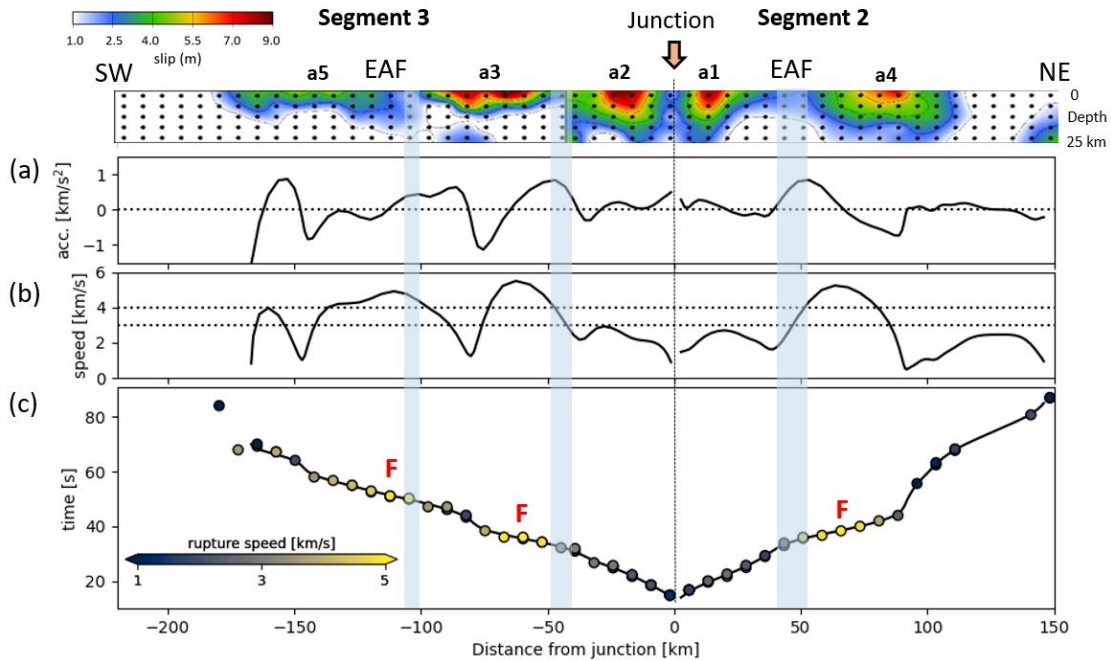


316

317 **Figure 4.** Time-distance plots of slip for segments 1 and 1bis **(a)** and for segments 2
 318 and 3 **(b)** from the joint inversion of strong motion and GNSS data. SPF: splay fault;
 319 EAF: East Anatolian Fault; orange dots: subfault timing at a function of distance, with
 320 size proportional to slip (larger than 1 m). Green shaded area: allowed domain for
 321 average rupture speed. Oblique black line: average rupture speed 3 km/s. Lines of
 322 average rupture speed start from the hypocenter in **(a)** and from the junction
 323 between the splay fault (segment 1) and the EAF (segment 2) in **(b)**. The slip
 324 distribution along strike and dip is shown above the graphs. On top of **(a)**, the
 325 position along strike of strong motion stations 4615 and NAR is indicated, and on

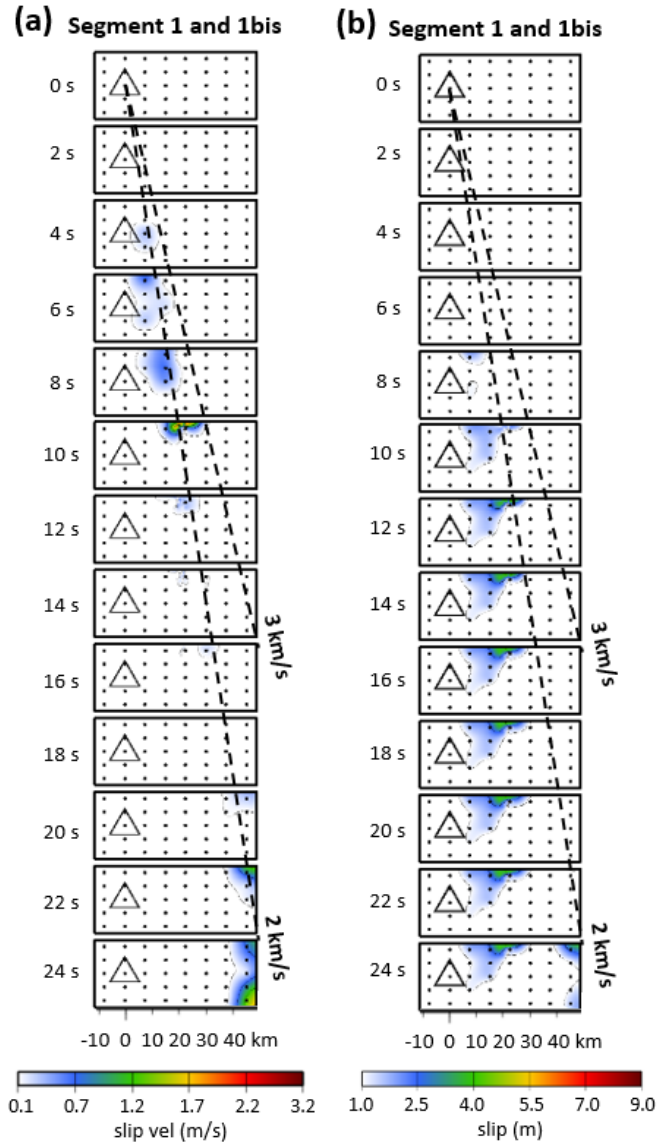
326 top of **(b)**, the junction with the splay fault is indicated by the orange arrow. a1 to
 327 a5: labels for the main slip areas along the EAF.

328



329

330 **Figure 5.** Estimation of rupture speed as a function of distance from the junction along
 331 the EAF (Segment 2 and 3). **(a)** Inverted rupture acceleration. **(b)** Local rupture speed
 332 (integral of acceleration). **(c)** Black curve: rupture onset time (related to the second
 333 integral of acceleration). The markers represent the observed onset times colored
 334 according to the estimated local rupture speed. Compared to Fig. 4b, only the
 335 subfaults whose time is less than 1 s from the rupture front at a given horizontal
 336 position are included in the inversion and panel c. The shaded regions indicate the
 337 locations of low slip. F (fast) markers in red point to areas of high local speed, reaching
 338 supershear. Slip map on top with the same labels as in previous Figures.



339

340

341

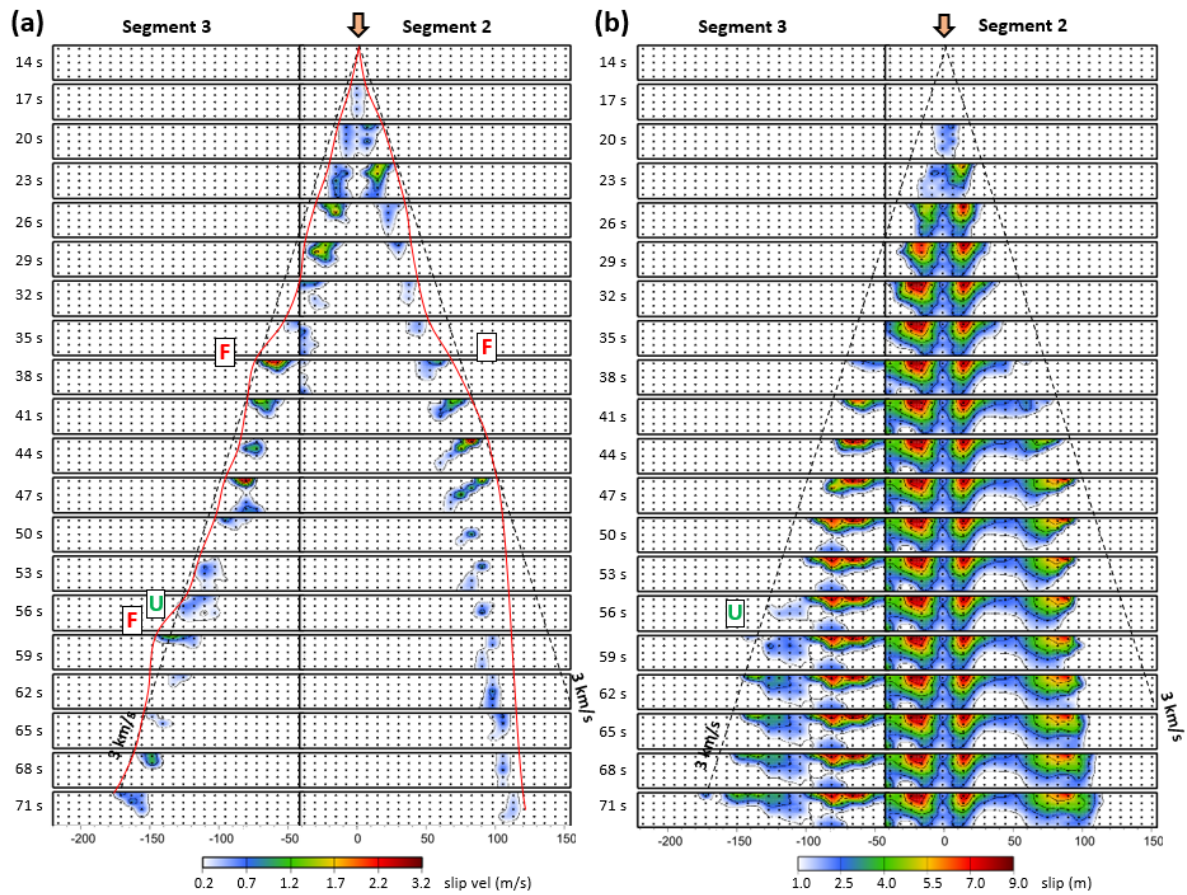
342

343

344

345

Figure 6. Snapshots of the space-time evolution of the rupture on segments 1 and 1bis (splay fault) from the joint inversion of strong motion and GNSS data. **(a)** slip velocity at each time step, **(b)** cumulative slip. Time steps are indicated on the left side. Open triangle: hypocenter. Oblique dashed black lines: reference slopes corresponding to average rupture velocities (V_r) 2 and 3 km/s, starting from the hypocenter.



346

347

348

349

350

351

352

353

354

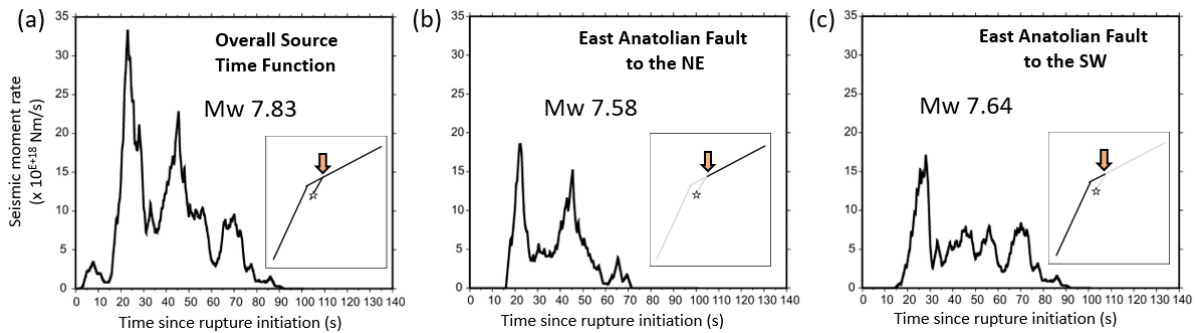
355

356

Figure 7. Snapshots of the space-time evolution of the rupture on segments 3 and 4 (EAF) from the joint inversion of strong motion and GNSS data. **(a)** slip velocity at each time step, **(b)** cumulative slip. Time steps are indicated on the left side. Oblique dashed black lines: reference slope corresponding to average rupture velocity (V_r) 3 km/s, starting from the junction with the splay fault (orange arrow). The red curve in **(a)** tracks the rupture front with its variations. Boxes labeled F (fast) in red point to areas of increased local V_r , reaching supershear, related to the F markers in **Figure 5c**. Box labeled U (underneath) in green indicates where the slip is moving below the near-surface area that will slip about 4 m in the following seconds.

357 The overall source time function is shown in **Figure 8a**, together with those corresponding to the
358 NE-ward part of the rupture (**Figure 8b**) and to the SW-ward part of the rupture (**Figure 8c**). The
359 total duration of the rupture is about 80 s, with the NE and SW parts contributing simultaneously
360 between 15 to 72s. The initial pulse on **Figure 8a** (0 – 15 s) is due solely to the splay fault. The
361 overall moment magnitude M_w is 7.83. The moment magnitudes of the NE part, the SW part, and
362 the splay fault are 7.58, 7.64, and 6.98, respectively.

363

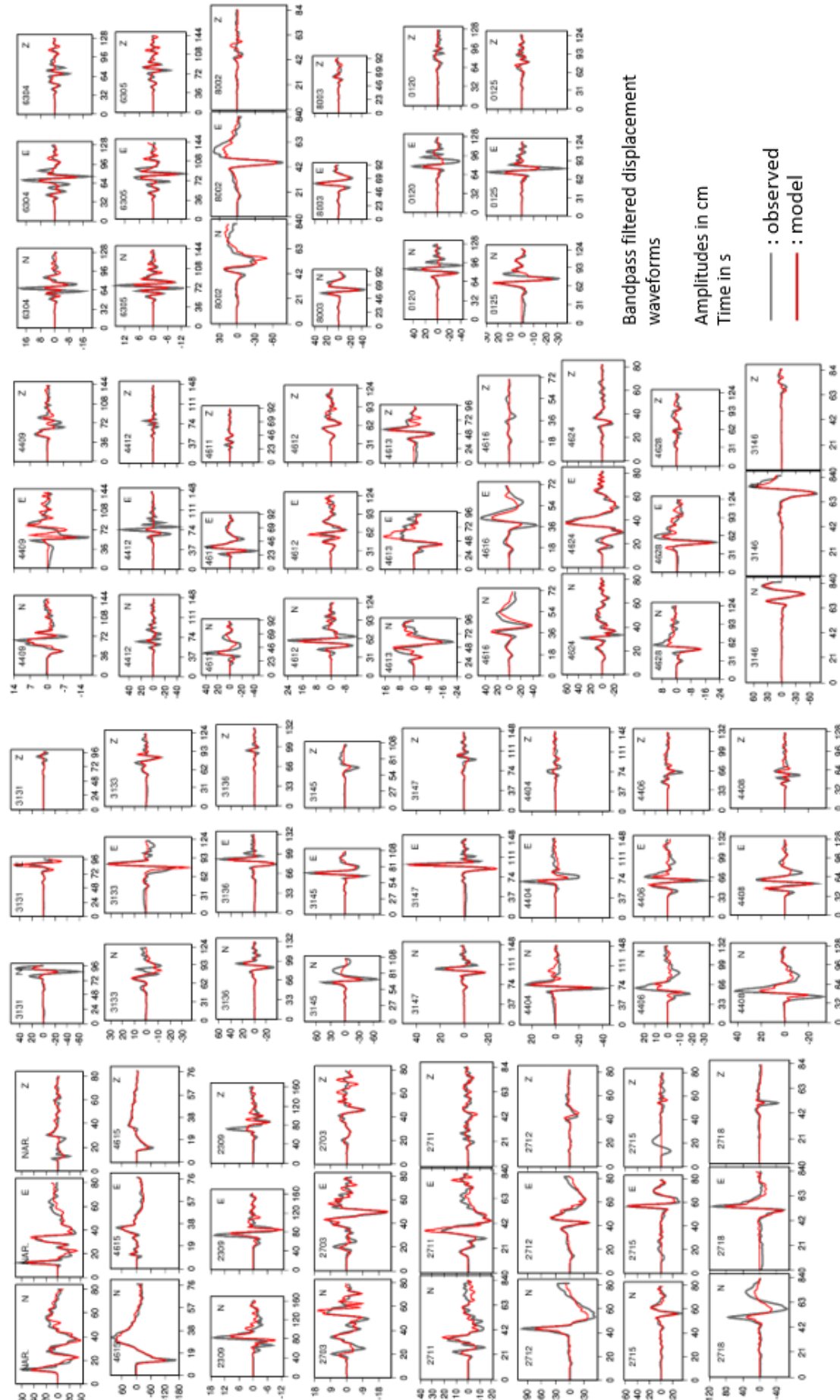


364

365 **Figure 8. (a)** Overall source time function (all rupture segments). **(b)** Source time
366 function for the part of the East Anatolian Fault rupturing to the North-East from
367 the junction with the splay fault. **(c)** Source time function for the part of the East
368 Anatolian Fault rupturing to the South-West from the junction with the splay
369 fault. The corresponding moment magnitude M_w is indicated in each case, and
370 the rupture segments involved are shown with heavy black lines in the inner
371 frame. Orange arrow: junction. Open star: epicenter. From the joint inversion of
372 strong motion and GNSS data.

373

374 The data fitting of the strong motion records integrated to displacement is shown on **Figure 9**,
375 and that of the horizontal GNSS offsets on **Figure 10**.



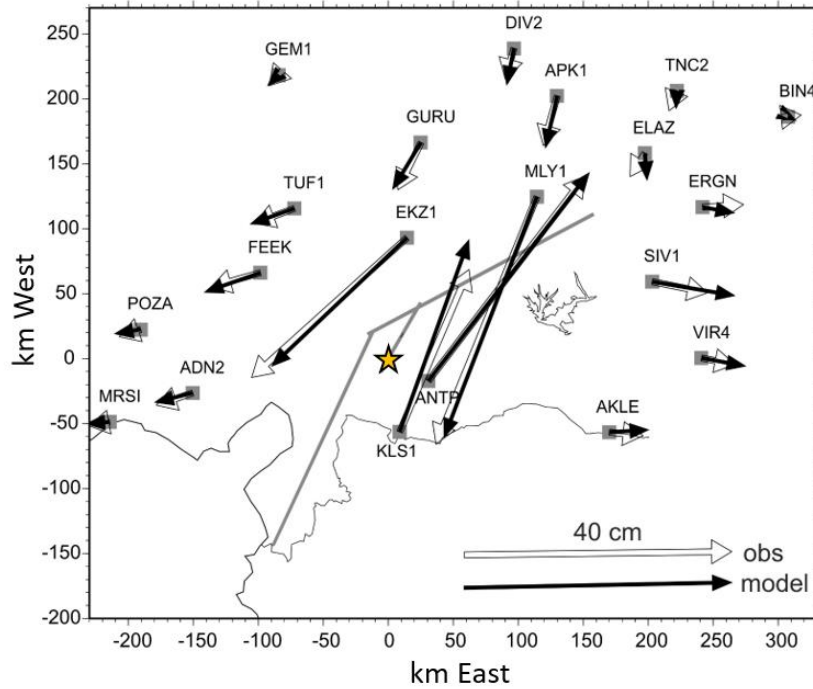
Bandpass filtered displacement waveforms

Amplitudes in cm
Time in s

— : observed
— : model

377 **Figure 9.** Waveform fitting by joint inversion of strong motion and GNSS data.
378 N, E, Z: north, east, vertical (up) components respectively. All displacement
379 waveforms bandpass filtered.

380



381

382 **Figure 10.** Horizontal GNSS offsets fitting by joint inversion of strong motion
383 and GNSS data. Orange star: epicenter. Heavy gray lines: trace of fault model.

384 Obs: observed.

385

386 Discussion

387 *Rupture velocity along the splay fault*

388 Rosakis et al. (2023) analyzed the records of strong motion stations NAR and 4615, integrated to
389 velocity and rotated to fault parallel (FP) and fault normal (FN) components with respect to the
390 splay fault assuming a strike of N22°. According to their analysis, based on theoretical and
391 laboratory experiments, the observed ratio FP/FN of 1.2 at station NAR is the signature of a
392 supershear rupture (FP/FN > 1). They further found that station 4615 is located at the transition
393 from sub-shear to supershear rupture.

394 Here, we find that ground displacement waveforms in the frequency band 0.01 to 0.3 Hz at
395 stations 4615 and NAR can be modeled correctly with a constant sub-shear rupture velocity on
396 the splay fault, as low as 2.5 km/s (**Figure 2a**). The question then arises whether the supershear
397 signature is present only on velocity signals, possibly only on unfiltered ones. In a first step, we
398 verified that the FP component of NAR is effectively larger than its FN component in velocity, both
399 on the unfiltered and on the 0.01 to 1 Hz bandpass filtered signals (**Figure S5** in the electronic
400 supplement to this article). This is illustrated for two possible azimuths of the splay fault, N22°
401 and N30°. In a second step, we verified that it is possible to model the velocity signals of both
402 stations NAR and 4615 without a transition to supershear (**Figure S6** in the electronic supplement
403 to this article). The modeling is done in the frequency band 0.01 to 1 Hz by finely discretizing the
404 rupture segment corresponding to the splay fault, but limiting its spatial dimensions to the
405 minimum necessary to model the first 15 s of signal, which include the main pulse associated with
406 the suspected supershear Mach front identified by Rosakis et al. (2023). The amplitude of the
407 main velocity pulse is correctly matched using a constant rupture velocity of 2.8 km/s all along
408 the splay fault, both on the N and E components and on the FP and FN components (**Figure S6** in
409 the electronic supplement to this article). We conclude that the criterion FP/FN > 1 is not

410 necessarily the signature of a supershear rupture, and that the main pulse observed in the initial
411 part of the records of stations NAR and 4615 can be explained by left-lateral shallow faulting
412 propagating at sub-shear velocity between the two stations.

413 The failure of the FP/FN criterion could be caused by a level of complexity of the rupture that has
414 not been accounted for in the underlying theoretical models and laboratory experiments. Indeed,
415 on the SPF the slip emerges at the surface at a substantial distance NE of the epicenter. This
416 pattern is reminiscent of the Mw 6.0 2014 South Napa, California earthquake, in which the
417 rupture propagated within a narrow corridor upward and obliquely from the hypocenter (Premus
418 et al., 2022). In contrast, the FP/FN criterion to distinguish sub-shear and supershear ruptures
419 arises from theoretical and experimental models with relatively more simple rupture front
420 geometries (Aagaard and Heaton, 2004; Dunham and Arhuleta, 2004; Bizzarri et al., 2010; Mello
421 et al., 2016).

422 *Resolution of the kinematic model*

423 We carried out a synthetic test to assess the resolution of the kinematic inversion. We designed
424 a synthetic kinematic model with variable slip and variable rupture velocity as shown in **Figure**
425 **S7-left** (slip distribution) and **Figure S8** (gray dots, rupture timing) in the electronic supplement
426 to this article. Based on this model, we generated synthetic displacement waveforms and static
427 offsets at the same strong motion and GNSS stations as for the real data. Amplitudes of the
428 synthetic data were randomly modified by a factor 1.1 or 0.9 at each station (10% change). These
429 modified synthetic data were inverted using exactly the same rupture parameterization and
430 algorithm than our real data inversion. However, we used a slightly modified 1D velocity model

431 to compute the Green's function (model of **Table S1** to generate the synthetic data, model of
432 **Table S2** for the inversion), to avoid unrealistically perfect conditions. Overall, the main features
433 of the synthetic model are retrieved. Nevertheless, there is some spreading of slip zones and
434 poorer timing resolution of moderate amplitude slip patches on the NE propagating portion of
435 the rupture, which can be related to the smaller number of stations and their relatively greater
436 distance from the rupture on this part of the source. We also observe an overestimation of the
437 subfault onset time at the NE termination of the splay fault. It can be assumed that the same
438 effects occur with the real data.

439 *Rupture transition from the splay fault to the East Anatolian Fault*

440 In our final model, rupture starts on the EAF at 14 s after the earthquake onset, before the
441 development of slip at the termination of the splay fault between 17 and 24 s (**Figure 4a and 6a**).
442 This suggests that rupture on the EAF was triggered before the end of rupture on the splay fault.
443 However, we have shown that a constant rupture speed of 3 km/s, or even a little faster, on the
444 splay fault produces an equally low RMS misfit of the data (**Figure 2**). At 3 km/s, the rupture arrives
445 at the junction with the EAF approximately 14 s after origin time, leading to a continuous rupture
446 from the splay fault to the EAF. We acknowledge an uncertainty of a few seconds on the timing
447 of the end of the rupture of the splay fault, as observed in the synthetic test. This uncertainty
448 could possibly be linked to a trade-off with the slip on the EAF at the junction, which in turn may
449 be due to the absence of strong motion stations very close to the junction.

450 *Necessity of local rupture speed variations*

451 To further evaluate whether rupture velocity variations along the EAF are indeed required by the
452 data, we performed an additional test in which a constant velocity of 3 km/s is imposed on
453 segments 2 and 3. The negative impact of this constant velocity assumption on waveform
454 modeling is clear at stations near the SW-ward rupture along segment 3 (**Figure S9** in the
455 electronic supplement to this article). The effect is less clear at stations around the NE-ward
456 rupture along segment 2. We conclude that variations in V_r are well-constrained by the data,
457 especially for the SW branch of the rupture, which is the best resolved part of the source owing
458 to the presence of several stations in close proximity.

459 *Comparison with other kinematic models*

460 Two kinematic models obtained by inversions of multiple data, including strong motion records,
461 have been published previously. These are the USGS finite fault model and that of Melgar et al.
462 (2023). The data used are not the same, although they partially overlap with each other and with
463 ours. While our study relies primarily on the dense network of strong motion instruments, the
464 two previous studies use a smaller subset of strong motion records and combine other data types
465 such as HR-cGNSS time series (which are not very close to the rupture), teleseismic data and InSAR
466 data. Note that Melgar et al. (2023) model both the Mw 7.8 and 7.6 earthquakes that occurred
467 on the same day in SE Turkey, which are covered by the same InSAR data.

468 Our kinematic model has in common several major features with the above mentioned models:
469 the initiation on the splay fault with moderate slip, followed by bilateral propagation on the EAF,
470 a more superficial rupture on the south-westernmost segment of the rupture, a maximum slip of
471 the order of 8 to 9 m on the EAF. We confirm that the average rupture velocity along the EAF did

472 not exceed about 3.2 km/s, as stated by Melgar et al. (2023). However, by modeling more strong
473 motion records, particularly the NAR and 4615 stations near the splay fault that were not
474 incorporated in previous studies, as well as other stations along the EAF, we find remarkable
475 features of rupture propagation that have not been fully addressed before, in particular the
476 existence of several portions where the rupture front propagates at supershear speeds along the
477 EAF.

478 *Transient supershear speeds*

479 The spatial fluctuations of local rupture speed are among the earthquake source properties that
480 are most difficult to constrain robustly, often due to scarcity of near-fault seismological data.
481 Transient supershear rupture was recently reported for the 2021 Mw 7.3 Madoi, China
482 earthquake using teleseismic back-projection analysis (Cheng et al., 2023), a technique that was
483 essential to reveal the steady supershear propagation of the 2018 Mw 7.5 Palu, Indonesia
484 earthquake (Bao et al., 2019). While systematic studies of global earthquakes show that
485 teleseismic back-projection can constrain well their average rupture speeds (Bao et al., 2022),
486 spatial fluctuations of rupture speed at scales of 10 km or less are best resolved with local strong
487 motion observations, as done in our present study.

488 Our source inversion results regarding rupture speed challenge simple models of dynamic
489 rupture. Theoretical models of steady ruptures with large aspect ratio (rupture length much larger
490 than rupture width), including supershear ruptures (Weng and Ampuero, 2020), predict a
491 correlation between final slip and rupture speed. We do not find such a correlation in our
492 inversion results (**Figure 5**). This implies that the exceptional dataset available for the 2023 Mw

493 7.8 Turkey earthquake warrants further extensions of current theories, which so far assume
494 simple rupture fronts or depth-averaged rupture properties (Weng and Ampuero, 2019). The
495 intermittent supershear bursts found here might result from 3D rupture patterns that cannot be
496 captured by 2.5D models. A possible scenario, proposed in dynamic rupture models by Dunham
497 et al (2003) and Page et al (2005), is a rupture front that reaches the edge of an asperity, goes
498 around it, then breaks it and generates a burst of rupture acceleration to supershear. The fine-
499 scale details of such a pattern may not be resolvable by kinematic source inversion, even though
500 its coarser effect on rupture speed is, and may warrant elucidation by dynamic source inversions
501 (e.g. Premus et al, 2022).

502

503 **Conclusions**

504 Taking advantage of the exceptional strong motion dataset made available by the Turkish Disaster
505 and Emergency Management Authority (AFAD), which had been used less comprehensively by
506 previous studies, and to a lesser extent of GNSS static data, we determine the rupture
507 characteristics of the February 6, 2023 Mw 7.8 earthquake in southeast Turkey.

508 We explore in detail the rupture properties required to model the seismograms recorded by two
509 stations, NAR and 4615, located very close to the splay fault on which the earthquake started. We
510 show that supershear rupture speed is not required on the splay fault. Indeed, these seismograms
511 can be correctly modeled, in displacement and in velocity, by a sub-shear rupture passing
512 between the two stations with about 4 m of slip at or near the surface.

513 About 14 s after rupture initiation, the rupture on the splay fault reached the East Anatolian Fault
514 (EAF). It then propagated bilaterally along the EAF, extending about 120 km NE and 180 km SW.
515 The depth extent of the rupture decreases as it passes the bend of the EAF to the SW. The highest
516 slip values are located near the surface on each rupture segment, with a maximum of 8 m +/- 2
517 m along the EAF.

518 The along-strike averaged rupture velocity remains below about 3.3 km/s, but locally, when
519 entering strong slip zones after crossing weak slip zones, the rupture velocity becomes supershear
520 for a few tens of kilometers. This pattern of rupture deceleration and acceleration is observed at
521 three different locations along the EAF, thanks to the exceptionally dense near-fault recordings
522 available.

523 Lateral progression of the rupture generally begins at or near the surface before propagating at
524 depth, with a notable exception in the south-westernmost part of the rupture where a slip patch
525 at the surface breaks after the rupture has surrounded it at larger depth.

526

527 **Acknowledgments**

528 B.D. and J.P.A. are partially funded by the EU project “A Digital Twin for Geophysical Extremes”
529 (DT-GEO, No. 101058129). J.P.A. is also funded by the French government through the UCA-JEDI
530 Investments in the Future project (ANR-15-IDEX-01) managed by the National Research Agency
531 (ANR). M.vdE is supported by the European Research Council (ERC) under the European Union’s
532 Horizon 2020 research and innovation programme (grant agreement No. 101041092 - ABYSS).

533

534 **Data and resources**

535 The strong motion data were retrieved from the Disaster and Emergency Management

536 Authority of Turkey (AFAD) - Disaster and Emergency Management Authority. (1973). Turkish

537 National Strong Motion Network [Data set]. Department of Earthquake, Disaster and Emergency

538 Management Authority <https://doi.org/10.7914/SN/TK>) using <https://tadas.afad.gov.tr/login>

539 <https://tadas.afad.gov.tr/list-event> (last accessed on February 16, 2023).

540 GPS data were retrieved from the Nevada Geodetic Laboratory (Blewitt et al., 2018) using

541 <http://geodesy.unr.edu/> (last accessed on 9 March 2023).

542 USGS Turkey Earthquake Emergency Response (Reitmann et al., 2023).

543 (<https://usgs.maps.arcgis.com/apps/webappviewer/index.html?id=5229bb842bd64b688d769ab>

544 [befe43b46](https://usgs.maps.arcgis.com/apps/webappviewer/index.html?id=5229bb842bd64b688d769ab)), last accessed on 9 March 2023.

545 Kahramanmaraş Supersite science web (<http://geo-gsni.org/kahramanmaras-supersite-science->

546 [page/](http://geo-gsni.org/kahramanmaras-supersite-science-)) (last accessed on March 9, 2023).

547 Some figures were partly made using the Generic Mapping Tools (GMT) package by Wessel et al.

548 (2019) (<https://www.generic-mapping-tools.org/>) (last accessed on April 17, 2023).

549 Seismic data processing was partly done using the Seismic Analysis Code (SAC) package by

550 Goldstein et al. (2003) and Goldstein and Snoke (2005)

551 (<http://ds.iris.edu/ds/nodes/dmc/software/downloads/sac/102-0/>) (last accessed on April 12,

552 2023).

553

554 **References**

555 Aagaard, B. T., and T. H. Heaton (2004). Near-source ground motions from simulations of
556 sustained intersonic and supersonic fault ruptures. *Bull. Seismol. Soc. Am.*, 94 (6), 2064-2078.

557 Bao, H., Ampuero, J. P., Meng, L., Fielding, E. J., Liang, C., Milliner, C. W., Feng, T., & Huang, H.
558 (2019). Early and persistent supershear rupture of the 2018 magnitude 7.5 Palu earthquake.
559 *Nature Geoscience*, 12(3), 200-205.

560 Bao, H., Xu, L., Meng, L., Ampuero, J. P., Gao, L., & Zhang, H. (2022). Global frequency of oceanic
561 and continental supershear earthquakes. *Nature Geoscience*, 15, 942–949.

562 Bizzarri, A., Dunham, E. M., & Spudich, P. (2010). Coherence of Mach fronts during heterogeneous
563 supershear earthquake rupture propagation: Simulations and comparison with observations.
564 *Journal of Geophysical Research: Solid Earth*, 115 (B8), B08301.

565 Blewitt, G., W. C. Hammond, and C. Kreemer (2018), Harnessing the GPS data explosion for
566 interdisciplinary science, *Eos*, 99, <https://doi.org/10.1029/2018EO104623>.

567 Bouchon, M. (1981). A simple method to calculate Green's functions for elastic layered media,
568 *Bull. Seismol. Soc. Am.*, 71 (4), 959–971.

569 Cheng, C., D. Wang, Q. Yao, L. Fang, S. Xu, Z. Huang, T. Liu, Z. Wang and X. Huang (2023). The
570 2021 Mw 7.3 Madoi, China Earthquake: Transient Supershear Ruptures on a Presumed Immature
571 Strike-Slip Fault. *Journal of Geophysical Research: Solid Earth*, 128 (2), e2022JB024641.

572 Delouis, B., D. Giardini, P. Lundgren, and J. Salichon (2002). Joint inversion of InSAR, GPS,
573 teleseismic and strong motion data for the spatial and temporal distribution of earthquake slip:

574 Application to the 1999 Izmit Mainshock, *Bull. Seism. Soc. Am.*, 92, 278-299.
575 <https://doi.org/10.1785/0120000806>

576 Delouis B., E. Oral, M. Menager, J.-P. Ampuero, A. Guilhem Trilla, M. Régnier, and A. Deschamps
577 (2021). Constraining the point source parameters of the 11 November 2019 Mw 4.9 Le Teil
578 earthquake using multiple relocation approaches, first motion and full waveform inversions,
579 *Comptes Rendus Géoscience* 353(S1):1-24. DOI : <https://doi.org/10.5802/crgeos.78>

580 Dunham, E. M., Favreau, P., & Carlson, J. M. (2003). A supershear transition mechanism for cracks.
581 *Science*, 299 (5612), 1557-1559.

582 Dunham, E. M., and R. J. Archuleta (2004). Evidence for a supershear transient during the 2002
583 Denali fault earthquake, *Bull. Seismol. Soc. Am.*, 94 (6B), S256-S268.

584 Goldstein, P., D. Dodge, M. Firpo, and L. Minner (2003). "SAC2000: Signal processing and analysis
585 tools for seismologists and engineers, Invited contribution to "The IASPEI International Handbook
586 of Earthquake and Engineering Seismology", Edited by WHK Lee, H. Kanamori, P.C. Jennings, and
587 C. Kisslinger, Academic Press, London.

588 Goldstein, P., and A. Snoke, (2005). "SAC Availability for the IRIS Community", *Incorporated*
589 *Institutions for Seismology* Data Management Center Electronic Newsletter.

590 Güvercin, S. E., H. Karabulut, A. Ö. Konca, U. Doğan, and S. Ergintav (2022). Active seismotectonics
591 of the East Anatolian Fault, *Geophysical Journal International*, Volume 230, Issue 1, Pages 50–69,
592 <https://doi.org/10.1093/gji/ggac045>

593 Johnson, L. (1974). Green's function for Lamb's problem, *Geophys. J. R. Astr. Soc.* 37, 99-131.

594 Legrand, D. (1995). Etude conjointe de la source d'une population de séismes tectoniques ou
595 volcaniques en champ proche : de la sismologie classique aux effets non linéaires, Ph.D. Thesis,
596 Université Louis Pasteur, Strasbourg (FR), 204 pp.

597 Mello, M., H. S. Bhat, and A. J. Rosakis (2016). Spatiotemporal properties of Sub-Rayleigh and
598 supershear rupture velocity fields: Theory and experiments. *Journal of the Mechanics and Physics*
599 *of Solids*, 93, 153-181.

600 Meng L., H. Bao, H. Huang, A. Zhang, A. Bloore, and Z. Liu (2018). "Double Pincer Movement:
601 Encircling Rupture Splitting During the 2015 Mw 8.3 Illapel Earthquake", *Earth and Planetary*
602 *Science Letters*, 495, pp. 164-173. <https://doi.org/10.1016/j.epsl.2018.04.057>

603 Page, M. T., E.M. Dunham, and J. M. Carlson, (2005). Distinguishing barriers and asperities in
604 near-source ground motion. *Journal of Geophysical Research: Solid Earth*, 110 (B11), B11302.

605 Premus, J., F. Gallovič, and J.-P. Ampuero (2022). Bridging time scales of faulting: From coseismic
606 to postseismic slip of the M w 6.0 2014 South Napa, California earthquake. *Science Advances*, 8
607 (38), eabq2536.

608 Reitman, N. G, R. W. Briggs, W. D. Barnhart, J. A. Thompson Jobe, C. B. DuRoss, A. E. Hatem, R. D.
609 Gold, J. D. Mejstrik, and S. Akçiz (2023) Preliminary fault rupture mapping of the 2023 M7.8 and
610 M7.5 Türkiye Earthquakes. DOI: <https://doi.org/10.5066/P985I7U2>

611 Rosakis, A., M. Abdelmeguid, and A. Elbanna (2023). Evidence of Early Supershear Transition in
612 the Mw 7.8 Kahramanmaraş Earthquake From Near-Field Records. *arXiv preprint*
613 arXiv:2302.07214. <https://arxiv.org/ftp/arxiv/papers/2302/2302.07214.pdf>

614 Savage, J. C. (1980). Dislocations in seismology, in Dislocations in solids, F. R. N. Navarro (Editor),
615 North-Holland, Amsterdam

616 USGS finite source model (2023).
617 <https://earthquake.usgs.gov/earthquakes/eventpage/us6000jllz/finite-fault>

618 Weng, H., & Ampuero, J. P. (2019). The dynamics of elongated earthquake ruptures. *Journal of*
619 *Geophysical Research: Solid Earth*, 124 (8), 8584-8610.

620 Weng, H., & Ampuero, J. P. (2020). Continuum of earthquake rupture speeds enabled by oblique
621 slip. *Nature Geoscience*, 13 (12), 817-821.

622 Wessel, P., J. F. Luis, L. Uieda, R. Scharroo, F. Wobbe, W. H. F. Smith, and D. Tian (2019). The
623 Generic Mapping Tools version 6. *Geochemistry, Geophysics, Geosystems*, 20, 5556–5564.
624 <https://doi.org/10.1029/2019GC008515>

625 Zhang, G., M. Vallée, X. Shan, and B. Delouis (2012). Evidence of sudden rupture of a large
626 asperity during the 2008 Mw7.9 Wenchuan earthquake based on strong motion analysis.
627 *Geophysical Research Letter*, L17303, doi:10.1029/2012GL052516.

628

629 **Mailing address of Authors:**

630 B.D., M.vdE, and J-P.A.: CNRS-GEOAZUR, Campus Azur, 250 rue Albert Einstein, CS 10269,
631 06905 Sophia Antipolis Cedex, France

632 Email address: delouis@geoazur.unice.fr, Martijn.VANDENENDE@oca.eu,

633 ampuero@geoazur.unice.fr

634